

# Conditional Diffusion Model with Anatomical-Dose Dual Constraints for End-to-End Multi-Tumor Dose Prediction

Hui Xie<sup>a,b</sup>, Haiqin Hu<sup>c</sup>, Lijuan Ding<sup>d</sup>, Qing Li<sup>b</sup>, Yue Sun<sup>a,\*</sup>, Tao Tan<sup>a,\*</sup>

<sup>a</sup>*Faculty of Applied Sciences, Macao Polytechnic University, R. de Luís Gonzaga Gomes, Macao, 999078, , P. R. China*

<sup>b</sup>*Department of Oncology, Affiliated Hospital of Xiangnan University, No.31 Renmin West Road, Chenzhou, 423000, Hunan, P. R. China*

<sup>c</sup>*Department of Oncology, Jiangxi Cancer Hospital, No. 519, Beijing East Road, Nanchang, 330029, Jiangxi, P. R. China*

<sup>d</sup>*Department of Oncology, Chenzhou Third People's Hospital, No. 8, Jiankang Road, Chenzhou, 423000, Hunan, P. R. China*

---

## Abstract

Radiotherapy treatment planning typically relies on labor-intensive, trial-and-error adjustments, making the process time-consuming and highly dependent on the expertise of dosimetrists. Existing deep learning approaches continue to face limitations in generalization across tumor types, prediction accuracy, and clinical applicability. To address these challenges, we propose ADDiff-Dose, an Anatomical-Dose Dual Constraints Conditional Diffusion Model for end-to-end multi-tumor dose prediction. The model incorporates a Lightweight 3D Variational Autoencoder (LightweightVAE3D) to compress high-dimensional CT data, and leverages multimodal inputs—including target and organ-at-risk (OAR) masks and beam parameters—within a progressive noise addition and denoising framework. Conditional features are integrated via a multi-head attention mechanism, while a composite loss function combining MSE, conditional, and KL divergence terms ensures both dosimetric accuracy and clinical constraint compliance. Evaluation on a large-scale public dataset (2,877 cases) and three external institutional cohorts (450 cases in total) demonstrates that ADDiff-Dose significantly outperforms conventional baselines, achieving a Mean Absolute Error (MAE) of 0.101–0.154, compared to 0.316 for UNet and 0.169 for GAN models. The model also achieves a DICE coefficient of 0.927, marking a 6.8% improvement, and limits spinal cord maximum dose error to within 0.1 Gy. Furthermore, the average plan generation time per case is reduced to 22 seconds. Ablation studies confirm that the structural encoder enhances compliance with clinical dose constraints by 28.5%. To our knowledge, this is the first work to introduce a Conditional diffusion model-based framework for radiotherapy dose prediction. The proposed method offers a generalizable and efficient solution for automated treatment planning across diverse tumor sites, with the potential to significantly reduce planning time and improve clinical workflow efficiency.

**Keywords:** Conditional Diffusion Model; Anatomical-Dose Dual Constraints; Dose Prediction; Multi-Tumor

---

## 1. Introduction

Cancer remains a leading cause of morbidity and mortality worldwide, posing a persistent threat to human health. Among the three principal treatment modalities—surgery, chemotherapy, and radiotherapy—approximately 80% of patients with malignant tumors require radiotherapy at some stage during their disease course [1]. The efficacy of radiotherapy hinges

on the precise formulation of treatment plans, which aim to maximize tumor cell eradication while sparing adjacent healthy tissues. This planning process typically demands experienced radiotherapy physicists to iteratively adjust beam parameters to generate clinically acceptable three-dimensional dose distributions, often assessed via dose-volume histograms (DVHs). However, manual planning is time-consuming and labor-intensive, usually taking several hours to days for a single case. Additionally, the final plan quality can vary significantly depending on the planner’s expertise, potentially limiting the individualization and optimality of treatment regimens [2].

In response, recent advances in deep learning have facilitated the development of data-driven models that automate dose prediction and streamline clinical workflows. Convolutional neural networks (CNNs), generative adversarial networks (GANs), and attention-based models have shown promise in learning mappings between anatomical features and dose distributions from historical datasets [3]. For example, ResNet101 has been employed to accurately predict dose for nasopharyngeal carcinoma by integrating anatomical and beam parameters with a multi-scale feature fusion mechanism [5, 4]. In the domain of lung cancer, the asymmetric A-Net architecture achieved clinically acceptable results in the 50–60 Gy range and delivered high spatial precision in mobile lesion regions [6, 7]. Traditional knowledge-based planning (KBP) approaches also remain relevant. Techniques combining kernel density estimation, k-nearest neighbors, and PCA have demonstrated the feasibility of dose modeling from limited clinical cohorts [8]. Despite encouraging progress, current methods face several limitations. First, most existing models are tailored to specific tumor types (e.g., prostate, head and neck) or limited to particular delivery techniques (e.g., IMRT, VMAT), limiting cross-domain generalization [7, 9]. Second, training data volumes remain relatively small (typically  $\leq 200$  patients), restricting model robustness to anatomical variability [10]. Third, prediction performance has yet to meet clinical gold standards: even advanced architectures like U-Net and 3D GAN exhibit mean absolute errors exceeding 1–3 Gy in certain regions or cases [11, 12].

In parallel, diffusion models have emerged as a powerful generative paradigm, achieving state-of-the-art performance across diverse domains such as image synthesis [56], fashion generation [57], and human motion modeling [48, 58]. Their ability to iteratively refine predictions through a learned denoising process offers unique advantages for generating complex, high-resolution outputs under multimodal constraints. However, while diffusion models have been widely adopted in computer vision, natural language processing, and other multimedia applications [49, 46, 47], their application to radiotherapy dose prediction remains relatively nascent. Only a handful of recent studies, such as DoseDiff [13] and MD-Dose [14], have begun exploring this avenue, highlighting a critical research gap in leveraging the strengths of diffusion models to handle the anatomical complexity and precision demands of radiotherapy.

To address these challenges, we propose ADDiff-Dose, an end-to-end anatomical-dose dual-constrained conditional diffusion framework for multi-tumor radiotherapy dose prediction. Our model incorporates CT images, organ and target contours, prior dose maps, and beam parameters as multimodal inputs to guide a conditional generative process. By integrating domain knowledge directly into the diffusion trajectory, ADDiff-Dose enables accurate and generalizable dose prediction for both head and neck and lung cancers under a unified architecture. Extensive experiments on multicenter datasets demonstrate its superiority in prediction accuracy, structural consistency, and cross-site adaptability, offering a promising solution for future intelligent radiotherapy planning. The innovation of this study is mainly reflected in the following five aspects:

1. **Breakthrough in technical application:** It pioneered the introduction of the Conditional Diffusion Model into the field of radiotherapy dose prediction, filling the gap in the application of

this technology in such scenarios. Compared with traditional generative models (such as GAN or U-Net), the proposed ADDiff-Dose model adopts the Progressive Noising and Denoising mechanism. It accurately guides the generation process of dose distribution by fusing multimodal inputs such as CT images, PTV/OAR masks, and beam parameters.

**2. Innovation in loss function:** To ensure both the fidelity of anatomical structures and the compliance of clinical doses, a Composite Loss Function is proposed. It "hard-codes" the professional knowledge in the radiotherapy field into the diffusion process, realizing the deep adaptation of the model to clinical constraints.

**3. Design for efficiency optimization:** Aiming at the computational bottleneck caused by high-resolution CT data, a lightweight 3D-VAE is innovatively designed. It achieves 99.7

**4. Expansion of generalization ability:** ADDiff-Dose realizes multi-tumor dose prediction under a unified framework for the first time, which can support IMRT/VMAT technologies for both head and neck cancer and lung cancer. It breaks through the limitations of traditional models in single tumor types or radiotherapy technologies.

**5. Improvement of clinical practicability:** Through the dose-volume constraints integrated with clinical prior knowledge, the dynamic balance between target coverage and organ at risk (OAR) protection is realized at the model level, effectively enhancing the clinical reference value of the prediction results.

## 2. Methods

Radiotherapy dose distribution prediction must simultaneously satisfy the dual requirements of anatomical structure fidelity and physical constraint compliance. To address the limitations of traditional unconditional diffusion models in integrating multimodal prior knowledge, this study proposes an end-to-end diffusion model based on anatomical-dose dual constraints. The model innovatively integrates multimodal inputs and prior-knowledge-guided diffusion mechanisms, enabling accurate dose prediction across tumor types within a unified architecture. The model comprises the following core components: a lightweight 3D variational autoencoder (LightweightVAE3D), a 3D UNet backbone network[16], a conditional embedding layer (ConditionalLayer), and a multi-head attention mechanism (MultiHeadAttention)[15] (Figure 1).

### 2.1. Lightweight 3D Variational Autoencoder (LightweightVAE3D)

To address the issue of dramatically increased computational complexity caused by the high resolution of the original CT images in radiotherapy dose prediction tasks, this study designed a lightweight 3D variational autoencoder (LightweightVAE3D)[17]. The model adopts a symmetric encoder-decoder architecture (Figure 2), and achieves a balance between computational efficiency and anatomical feature preservation through joint optimization of feature compression and reconstruction.

**Encoder Design:** The encoder employs a four-layer 3D convolutional chain (kernel size:  $4 \times 4 \times 4$ , stride: 2, padding: 1, activation function: StableSiLU) to perform progressive down-sampling. The number of input channels increases gradually from 1 to 256 (channel expansion ratio: 1:256), enabling the model to capture hierarchical image information through multi-scale feature extraction. Ultimately, the original CT images (with a resolution of  $96 \times 128 \times 144$  voxels) are compressed into a low-dimensional latent space of  $6 \times 8 \times 9$  voxels, achieving a dimensionality reduction of approximately 99.7%. At the end of the encoder, fully connected layers output the Gaussian distribution parameters — mean ( $\mu$ ) and variance ( $\sigma^2$ ) — of the latent space. These parameters provide the probabilistic foundation for the subsequent diffusion process.

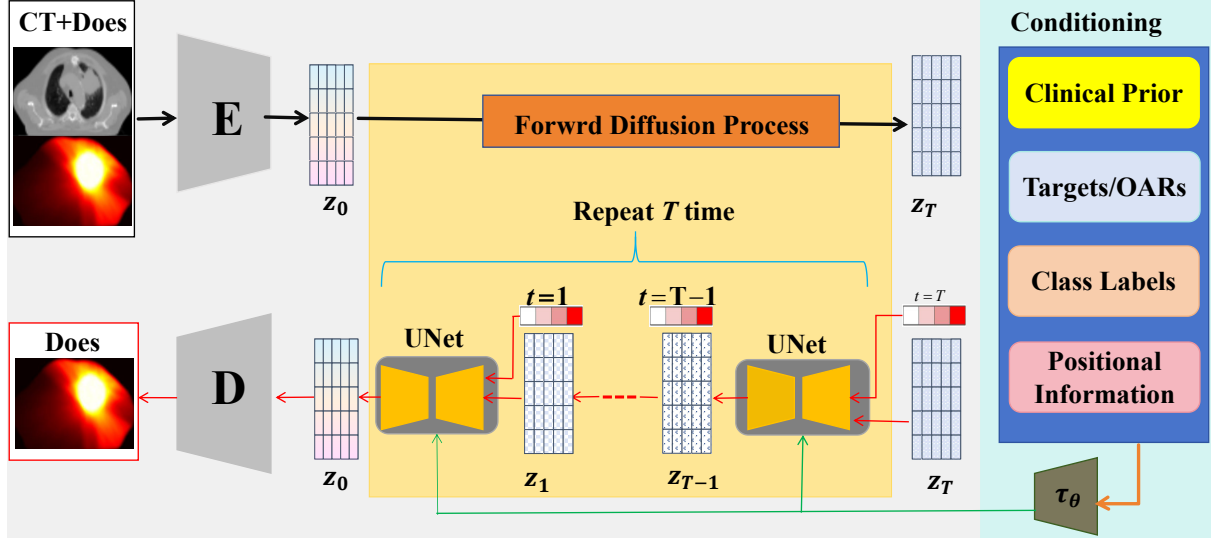


Figure 1: Overall Framework of the Model Proposed in This Study. The framework adopts a left-to-right horizontal data flow design, structured into five core modules: the Input Module, Variational Autoencoder (VAE), Forward Diffusion Process, Conditioning Information Flow, and U-Net (network architecture).

**Decoder design:** The decoder employs a symmetric 3D transposed convolution chain to gradually upsample and restore image resolution. The number of output channels decreases from 256 to 1, adapting to the normalized CT value range of  $[0, 1]$ . A Sigmoid activation function is introduced to constrain the reconstructed value range, avoiding numerical overflow issues and ensuring the accuracy of anatomical structure reconstruction and clinical rationality.

**Training optimization strategy:** During the training phase, reparameterization techniques are introduced to enhance gradient propagation efficiency. The model jointly optimizes the adversarial loss and the reconstruction loss ( $L_{VAE} = \|\tilde{x} - x\|_1 + \beta D_{KL}(q(z|x)||p(z))$ ). Here, the Kullback-Leibler (KL) divergence  $D_{KL}$  adjusts the weight coefficient  $\beta$  through a dynamic annealing strategy, achieving progressive regularization of the latent space distribution. This strategy reduces computational load while successfully preserving the morphological features of the target area and organs at risk, providing high-quality anatomical priors for subsequent diffusion models.

## 2.2. Conditional Diffusion Model

### 2.2.1. Multi-Source Conditional Feature Construction

After being processed by the VAE encoder, the 3D CT image generates a 32-dimensional latent vector  $z_0$ , which serves as the initial input for the diffusion process. Simultaneously, channel merging operations are performed on the planning target volume (PTV) mask and the organs-at-risk (OAR) masks to generate a multi-channel structural tensor. Subsequently, 3D convolutional projection is applied to this structural tensor to form the conditional feature  $C$ . For discrete time steps  $t \in [0, 999]$ , they are mapped into high-dimensional temporal feature vectors  $temb$  through a time embedding function, thereby capturing the dynamic evolution characteristics during the diffusion process.

### 2.2.2. Progressive Noising and Denoising Mechanism

The noising process follows the Markov chain rule[18], using a linearly scheduled noise coefficient  $\beta_t$  (whose values range from  $10^{-4}$  to 0.02), progressively injecting Gaussian noise into the latent vector:

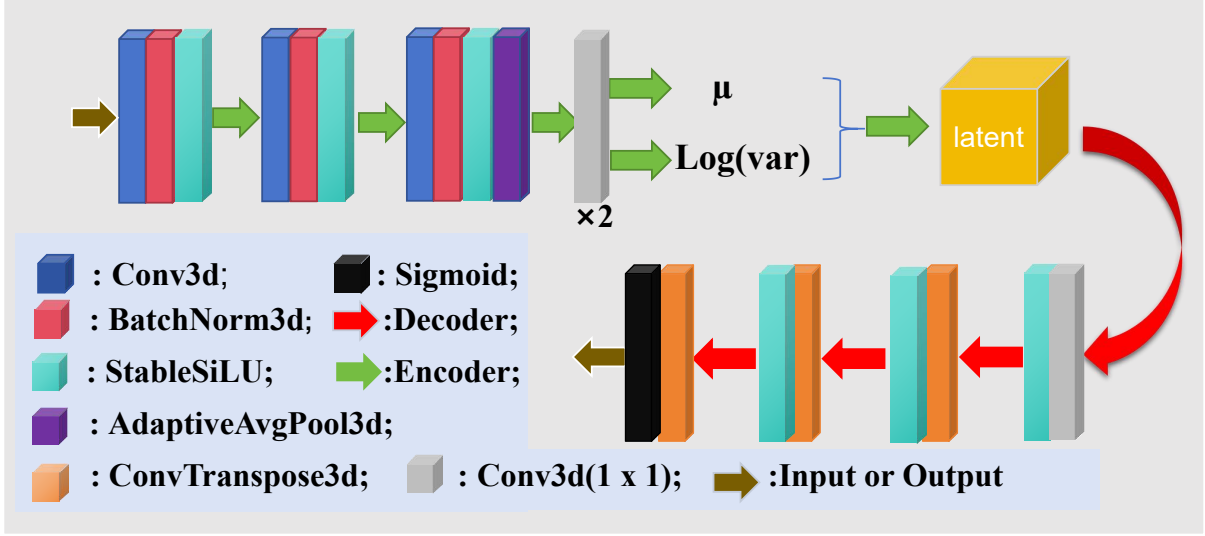


Figure 2: Figure 2: Architecture Diagram of the Variational Autoencoder (VAE). The upper encoding process uses layers like Conv3d, BatchNorm3d, StableSiLU, and AdaptiveAvgPool3d to generate  $\mu$  and  $\text{Log}(\text{var})$  for sampling the latent representation. The lower decoding process leverages ConvTranspose3d, StableSiLU, and Sigmoid layers to reconstruct output from the latent space, illustrating the full VAE workflow.

$$z_t = \sqrt{\alpha_t} z_{t-1} + \sqrt{1 - \alpha_t} \varepsilon_{t-1}, \quad \text{where } \alpha_t = 1 - \beta_t, \quad \varepsilon_{t-1} \sim \mathcal{N}(0, I).$$

Through this process, the original signal  $Z_0$  gradually degrades to Gaussian noise  $Z_T$ .

The reverse denoising process is implemented by a 3D UNet (UNet3D) (Figure 3). This UNet adopts an encoder-decoder architecture, consisting of 4 layers of downsampling (channel numbers increasing from 64 to 512) and 4 layers of upsampling (channel numbers decreasing from 512 to 64), and fuses multi-scale features through skip connections. In the deeper layers, a multi-head attention mechanism is introduced.

The UNet takes the noisy vector  $Z_t$ , time embedding  $t_{emb}$ , and conditional feature  $C$  as inputs, predicting the noise  $\varepsilon_\theta(z_t, t, C)$ , and then recovers the true signal through the recursive formula:

$$z_{t-1} = \frac{1}{\sqrt{\alpha_t}} \left( z_t - \frac{1 - \alpha_t}{\sqrt{1 - \alpha_t^{\text{cum}}}} \varepsilon_\theta(z_t, t) \right) + \sqrt{\beta'_t} \varepsilon,$$

where  $\alpha_t^{\text{cum}}$  is the cumulative noise coefficient, and  $\beta'_t$  is the adjusted noise variance, used to recover the true signal.

### 2.2.3. Anatomical Condition Fusion Mechanism

The conditional feature  $C$  and the time embedding  $t_{emb}$  interact through the conditional embedding layer. First, the dimensionality of the structural tensor is compressed using  $1 \times 1$  convolution. Then, cross-attention calculation is performed through Transformer blocks[19]. Finally, feature fusion is achieved with the aid of the multi-head attention mechanism. This mechanism ensures that the diffusion process is fully aware of the distribution of anatomical structures, thereby guiding the dose distribution to comply with clinical constraints, such as the maximum dose to the Spinal cord  $D_{max} \leq 45$  Gy, the Lung  $V_{20} \leq 30\%$ , etc. ( Supplementary Table 1).

### 2.3. Loss Function

The composite loss function designed in this study consists of three core components, which are optimized through multi-component collaborative optimization mechanisms to ensure that

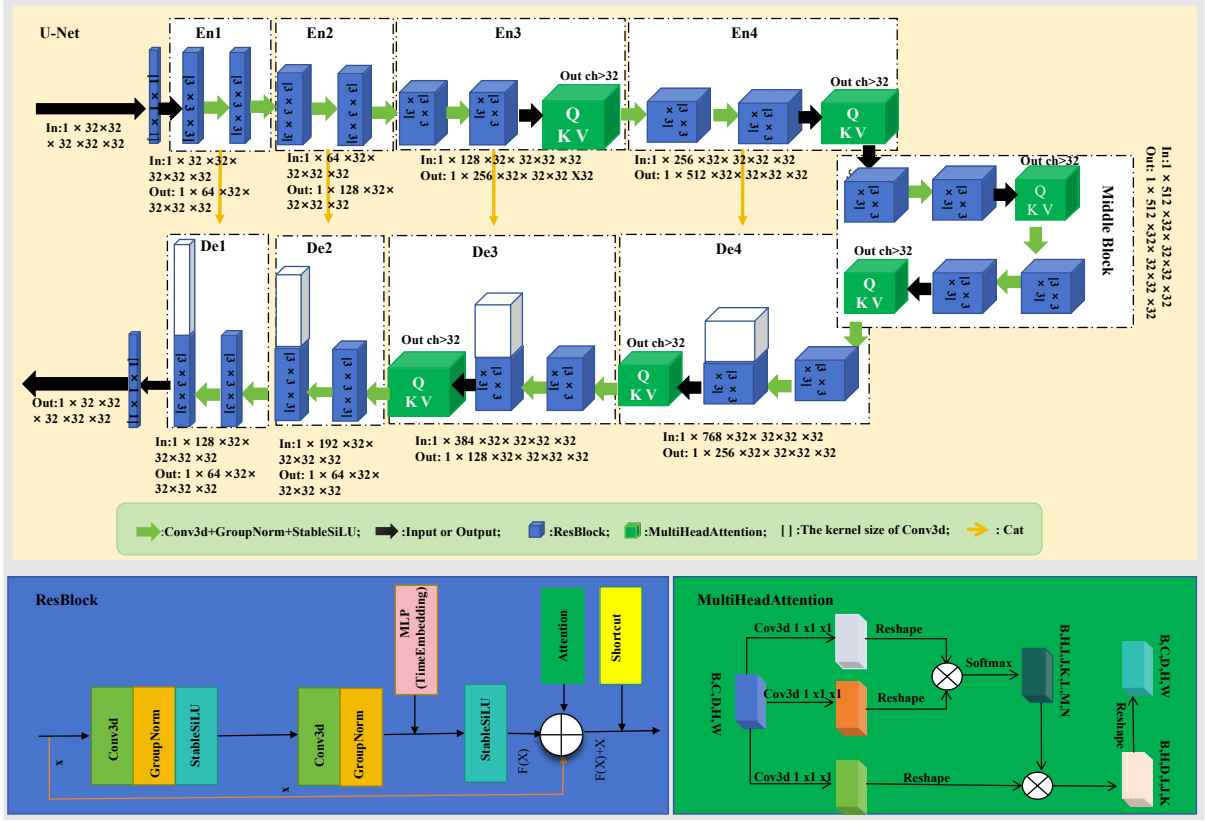


Figure 3: Architecture Diagram of the U-Net Model with Modified Attention and ResBlock Components. It shows the encoding (En1-En4) and decoding (De1-De4) paths, incorporating elements like Cascade - GroupNorm - StableSiLU, ResBlock, and MultiHeadAttention, along with detailed internal structures of ResBlock and MultiHeadAttention at the bottom.

the generated radiotherapy dose distribution is consistent with the anatomical structure while strictly satisfying clinical compliance requirements. The formula is expressed as:

$$L = \lambda_1 \cdot L_{mse} + \lambda_2 \cdot L_{cond} + \lambda_3 \cdot L_{kl}.$$

1. **Reconstruction Loss ( $L_{mse}$ )**: The reconstruction loss  $L_{mse}$  measures the difference between the predicted noise by UNet3D and the actual added noise, thereby driving the learning process of the "noise-to-dose" mapping. It is defined as:

$$L_{mse} = E_{t,z,C} [\|\epsilon_\theta(z_t, t, C) - \epsilon\|^2].$$

Where:  $z_t$ : The latent vector at time step  $t$  (generated by 3D-VAE encoding); -  $C$ : Conditional features combining the planning target volume (PTV) mask, organs-at-risk (OAR) masks, and time embeddings;  $\epsilon \sim \mathcal{N}(0, I)$ : Standard Gaussian noise.

2. **Clinical Dose Constraint Loss ( $L_{cond}$ )**: The clinical dose constraint loss  $L_{cond}$  integrates over 50 clinical constraints (Supplementary Table 1), categorized into two types:

(1) **OAR Protection Constraints**

Maximum Dose Constraint ( $D_{max}$ ): For example, the maximum dose for the spinal cord should not exceed 45 Gy. The loss term is defined as:

$$L_{D_{max}-OAR} = \max(0, \frac{\max(D - M_{(j)})}{\text{threshold}_{D_{max}-OAR}} - 1)^2,$$

where  $M_{(j)}$  represents the threshold value for organ  $j$ .

Volume Dose Constraint ( $V_x$ ): For example, the  $V_{20}$  for the lung should not exceed 30% . The loss term is defined as:

$$L_{V_x-OAR} = \max(0, \frac{\text{vol}(D \cdot M_O \geq 20 \text{ Gy})}{\text{vol}(M_O)} - 0.30)^2.$$

**(2) PTV Coverage Constraints :** Dose Coverage Constraint  $D_{95}$ : For example, the  $D_{95}$  for the PTV should not be lower than 95% of the prescribed dose. The loss term is defined as:

$$L_{D_{95}-PTV} = \max(0, 1 - \frac{D_{95}(PTV)}{\text{prescription} \times 0.95})^2,$$

all constraint terms are weighted according to clinical priority and summed up, expressed as:

$$L_{cond} = \sum_{o \in OAR} w_o \cdot (L_{D_{max-o}} + L_{V_x-o}) + \sum_{p \in PTV} w_p \cdot L_{D_{95-p}},$$

where  $w_o$  and  $w_p$  are weights set by radiation oncologists based on clinical experience (e.g., the weight for spinal cord  $D_{max}$  is higher than that for lung  $V_{20}$ ), and the constraints are only activated when the corresponding organ exists.

**(3) VAE Regularization Loss ( $L_{kl}$ ) :** The VAE regularization loss  $L_{kl}$  is only enabled during the pre-training phase of the 3D-VAE, where it ensures that the latent space distribution approximates a standard Gaussian distribution. This loss is defined as:

$$L_{kl} = \frac{1}{2} \mathbb{E} \left[ \sum_{i=1}^n (\sigma_i^2 + \mu_i^2 - 1 - \log \sigma_i^2) \right],$$

where  $\mu$  and  $\sigma^2$  are the mean and variance of the latent space generated by the VAE encoder. This loss ensures that the extracted anatomical features have good distribution properties, providing high-quality feature bases for the diffusion model.

During the pre-training phase, both  $L_{mse}$  (reconstruction loss) and  $L_{kl}$  are optimized simultaneously to improve the quality of feature extraction. In the end-to-end training phase, the design ensures feature quality through  $L_{kl}$ , while  $L_{mse}$  and  $L_{cond}$  work together to ensure that the generated dose distribution is highly consistent with the CT anatomy and strictly satisfies clinical constraints, providing a reliable optimization target for radiotherapy dose prediction.

#### 2.4. Training Details

This study implements a two-stage training strategy on a single NVIDIA RTX 4090 GPU (with 24GB of video memory) based on the PyTorch deep learning framework[20]. It integrates mixup data augmentation[21] and patch-based processing techniques[62] to enhance the model's generalization ability and effectively address the memory bottleneck caused by 3D medical imaging data.

Stage 1: Pre-training the Lightweight 3D Variational Autoencoder (LightweightVAE3D). The Adam optimizer is employed (with an initial learning rate of 1e-3, which gradually decays to 1e-5 via cosine annealing). The batch size is set to 8, and training is conducted for 200 epochs. During training, the mixup data augmentation strategy (with a mixing coefficient  $\alpha = 0.4$ ) is introduced to randomly mix CT image samples and their latent features, thereby enhancing data diversity. Additionally, for high-resolution 3D medical images, a patching strategy with voxel dimensions of 32×32×24 (with an overlapping region of 8×8×8) is adopted to reduce video memory usage and improve training efficiency.

Stage 2: Training the Conditional Diffusion Model. Based on fixed VAE encoder parameters, the AdamW optimizer is used (with an initial learning rate of  $5e-4$ , which cosine-anneals to  $1e-6$ ). The batch size is set to 2, and training is carried out for 1000 epochs. The diffusion process sets a total number of steps  $T = 1000$ , with the noise coefficient  $\beta_t$  linearly increasing from  $1e-4$  to 0.02, ensuring the smoothness and controllability of the noise addition process. During training, the mixup augmentation strategy is also applied to dynamically mix dose distribution samples and structural masks (with a mixing coefficient  $\text{lam} = 0.4$ ), further enhancing the model’s robustness and generalization ability.

To address the memory limitations of 3D data, the input data follows a ”patch - process - merge” workflow: the data is divided into patches of size  $32 \times 32 \times 24$ , with an overlapping region of  $8 \times 8 \times 8$  between adjacent patches. After prediction, a linearly decaying weighted merging strategy is used to fuse the overlapping regions, avoiding boundary effects. The entire training process is optimized end-to-end using the composite loss function  $L = \lambda_1 \cdot L_{mse} + \lambda_2 \cdot L_{cond}$  (which includes the weighted sum of the  $L_{mse}$  reconstruction loss and the  $L_{cond}$  loss with over 50 clinical dose constraints). Each training cycle fully traverses the training set and validation set, combined with an early stopping mechanism: if the clinical dose compliance rate does not improve for 20 consecutive epochs, training is terminated early. The entire training process takes approximately 200 hours. Through the synergistic effects of the aforementioned data augmentation, patching strategy, and multi-objective optimization mechanism, not only is the model’s generalization ability significantly enhanced, but the computational resource bottleneck of 3D medical data is also successfully addressed. Ultimately, simultaneous convergence of dose distribution prediction in terms of both anatomical structure adherence and clinical compliance is achieved.

For a clearer understanding, the training procedure is summarized in Algorithm 1.

### 3. Experiments and Results

#### 3.1. Dataset and Evaluations

In this study, the model was trained and internally validated using data from the AAPM GDP-HMM Dose Prediction Challenge (2025)[23] [24] [25]. To evaluate the generalization ability of the model, we conducted external testing on three private datasets: one from Xiangnan College Affiliated Hospital (comprising 300 patients who received radiotherapy), another from The Third People’s Hospital of Chenzhou City (including 50 treated patients), and the third from Jiangxi Cancer Hospital (containing 100 patients undergoing radiotherapy). Detailed information about the data is provided in Table 1. For each patient, the datasets include the computed tomography (CT) images, planning target volume (PTV) segmentation maps, organs-at-risk (OARs) segmentation maps, and the clinically delivered dose distributions. In our study, the clinical dose distribution information was incorporated to ensure consistency between anatomical and dosimetric features. All 3D images (including CT images) were resampled and cropped/padded to a standard size of  $96 \times 128 \times 144$  voxels. CT values were normalized to the range  $[-1000, 1000]$  and then divided by 500. Dose distributions were normalized based on the 3rd percentile value of the high-dose region within the PTV and divided by a factor of 10. In the internal dataset, all planning target volumes (PTVs) and organs-at-risk (OARs) were contoured by experienced radiation oncologists, and all radiotherapy plans have been clinically approved.

We employed the following evaluation metrics to quantitatively analyze the model performance: for the target region, if multiple targets were present, the target receiving the highest dose was selected as the representative. The evaluation metrics included the Mean Absolute Error (MAE), Dice Similarity Coefficient (DICE), and the 95th percentile Hausdorff distance



Table 1: Summary of Clinical Datasets Used in This Study

Dataset Source	N	Technique		Disease Type	
		IMRT	VMAT	Lung	Head & Neck
AAPM GDP-HMM 2025 (Public) [23, 24, 25]	2877	1646	1231	1454	1423
The Affiliated Hospital of Xiangnan University	300	150	150	150	150
Chenzhou Third Hospital	50	25	25	25	25
Jiangxi Cancer Hospital	100	50	50	50	50

*Note.* IMRT: Intensity-Modulated Radiation Therapy; VMAT: Volumetric Modulated Arc Therapy. All private datasets were collected between 2022-2024 with IRB approval.

(HD95). Specifically, MAE quantifies the overall accuracy of dose delivery by calculating the mean absolute difference between the predicted and the actual dose distributions. The DICE coefficient evaluates the spatial similarity between the predicted and the ground-truth dose distributions based on the ratio of overlapping volume to the union volume. HD95 measures the maximum one-sided distance between the predicted and the true contours at the 95th percentile, reflecting their proximity in spatial localization (Table 2). Notably, in scenarios involving multiple targets, selecting the highest-dose PTV as the evaluation focus aims to concentrate on the region with the steepest dose gradient and the most stringent requirements for dose accuracy. This ensures the clinical relevance of the evaluation results and enhances the sensitivity of the metrics.

To comprehensively and in - depth evaluate the performance of the proposed model, we additionally utilized a variety of evaluation indicators. For the target volume, we focused on key indicators such as D98, D2, maximum dose (Dmax), mean dose (Dmean), homogeneity index (HI), and conformity index (CI). These indicators can reflect the model’s performance in target volume dose prediction from different dimensions (Table 3).

For OARs, we adopted maximum dose, mean dose, the minimum dose delivered to a specific percentage of the structure ( $D_{x\%}$ ), and the percentage of the structure volume that receives at least a specific dose ( $V_{xGy}$ ) as evaluation indicators. These indicators help us understand the model’s ability to protect organs at risk. In this study, we selected particularly important organs at risk, including the spinal cord, brainstem, whole lungs, heart, and esophagus, for evaluation (Table 3). As shown in the DVH diagram (Figure 6).

### 3.2. Comparison with State-Of-The-Art Methods

To verify the performance advantages of the proposed model in dose prediction tasks, we conducted a comprehensive comparison with current mainstream advanced models, including UNet[26], GAN[27], DeepLabV3+ [28], and DoesNet [29]. The experimental results, as shown in Tables 3 and 4, demonstrate that the proposed model exhibits significant advantages across multiple core metrics. In terms of the MAE metric, the error values of the proposed model on the public dataset, Xiangnan University Affiliated Hospital, Chenzhou Third People’s Hospital, and Jiangxi Provincial Cancer Hospital are 0.101, 0.103, 0.139, and 0.154, respectively, all lower than those of other compared models (e.g., DoesNet has an MAE of 0.156 on the public dataset). Notably, on the two key metrics of  $\Delta HI$  ( $0.038 \pm 0.004$ ) and  $\Delta D98$  ( $0.024 \pm 0.011$ ), compared to DoesNet, which ranked second ( $\Delta HI = 0.042 \pm 0.018$ ,  $\Delta D98 = 0.032 \pm 0.017$ ), the proposed model reduced the values by 0.004 and 0.008, respectively, showing a significant improvement in error control capability. Additionally, on the  $\Delta D2$  ( $0.001 \pm 0.001$ ) and  $\Delta Dmax$  ( $0.0005 \pm 0.0006$ ) metrics, the values of the proposed model are only 1/10 to 1/3 of those of

Table 2: Comparison of Dose Prediction Performance Metrics of Multiple Models on Datasets of Different Medical Institutions

Methods	Performance Metrics			
	MAE	DICE	HD95 (mm)	Time (s)
<b>AAPM GDP-HMM 2025 (Public)</b>				
Unet[26]	0.316***	0.439**	10.439**	5.370**
GAN[27]	0.169	0.847*	11.854**	7.457**
deepLabV3[28]	0.297*	0.602*	17.143**	7.054**
DoesNet[29]	0.156*	0.859*	9.148*	8.443**
Baseline	0.150*	0.882*	9.075*	13.301*
Proposed	<b>0.101</b>	<b>0.927</b>	<b>8.947</b>	22.504
<b>The Affiliated Hospital of Xiangnan University</b>				
Unet[26]	0.305***	0.428***	23.348***	4.135***
GAN[27]	0.170*	0.835*	15.254**	7.100**
deepLabV3[28]	0.225**	0.715*	17.054**	7.067**
DoesNet[29]	0.155*	0.882*	10.117*	8.792**
Baseline	0.148*	0.876*	10.218*	13.324*
Proposed	<b>0.103</b>	<b>0.931</b>	<b>8.672</b>	23.216
<b>Chenzhou Third People's Hospital</b>				
Unet[26]	0.331***	0.483***	23.378	6.294**
GAN[27]	0.178*	0.823	15.891	7.672**
deepLabV3[28]	0.313***	0.564**	16.254	7.293**
DoesNet[29]	0.171*	0.819	11.082	8.037**
Baseline	0.164*	0.833	10.992	13.280*
Proposed	<b>0.139</b>	<b>0.897</b>	<b>9.217</b>	25.726
<b>Jiangxi Provincial Cancer Hospital</b>				
Unet[26]	0.228**	0.676**	21.054***	5.764***
GAN[27]	0.217**	0.831*	15.920*	7.672**
deepLabV3[28]	0.476***	0.479***	23.376**	10.295**
DoesNet[29]	0.169	0.872	10.081*	8.397**
Baseline	0.173*	0.838*	10.692*	14.067*
Proposed	<b>0.154</b>	<b>0.894</b>	<b>9.662</b>	25.982

Note: Bold values indicate best performance in each category.

\* $p < 0.05$ , \*\* $p < 0.01$ , \*\*\* $p < 0.001$  denote statistical significance levels compared with proposed method.

**Metrics Explanation:**

MAE (Mean Absolute Error): Dose prediction accuracy (Gy), lower is better.

DICE (Dice Similarity Coefficient): Spatial agreement (0-1), higher is better.

HD95 (95% Hausdorff Distance): Shape agreement (mm), lower is better.

Time (s): Computation time per case.

Table 3: Comparison of Dose Prediction Performance Metrics of Multiple Models on Datasets of Different Medical Institutions

Methods	$\Delta$ HI	$\Delta$ D98	$\Delta$ D2	$\Delta$ Dmax	$\Delta$ V20 (Lung)%	$\Delta$ V30 (Heart)%	$\Delta$ Dmax (Brainstem) Gy(Spinal cord)	$\Delta$ Dmax Gy(Esophagus)	$\Delta$ V30
AAPM GDP-HMM 2025 (Public)									
Unet[26]	$0.076 \pm 0.015^{**}$	$0.152 \pm 0.008^{**}$	$0.197 \pm 0.0022^{**}$	$0.215 \pm 0.0024^{**}$	$2.151 \pm 0.524^*$	$3.454 \pm 0.215$	$0.661 \pm 0.052$	$0.152 \pm 0.041$	$0.116 \pm 0.082$
GAN[27]	$0.042 \pm 0.031^*$	$0.037 \pm 0.015^*$	$0.083 \pm 0.0035^{**}$	$0.155 \pm 0.0017^{***}$	$1.576 \pm 0.211$	$3.044 \pm 0.106$	$0.196 \pm 0.013$	$0.196 \pm 0.029$	$0.111 \pm 0.065$
deepLabV3[28]	$0.051 \pm 0.026^*$	$0.091 \pm 0.024^{**}$	$0.043 \pm 0.0014^{**}$	$0.183 \pm 0.0009^{***}$	$1.683 \pm 0.212^*$	$3.128 \pm 0.198$	$0.211 \pm 0.032^*$	$0.187 \pm 0.040$	$0.187 \pm 0.040$
DoesNet[29]	$0.042 \pm 0.018^*$	$0.032 \pm 0.017^*$	$0.012 \pm 0.0007^*$	$0.011 \pm 0.00013^{***}$	$1.325 \pm 0.151$	$3.874 \pm 0.151$	$0.166 \pm 0.025^*$	$0.182 \pm 0.051$	$0.182 \pm 0.051$
Baseline	$0.037 \pm 0.026$	$0.046 \pm 0.036^*$	$0.008 \pm 0.00007$	$0.0051 \pm 0.0006^*$	$1.855 \pm 0.124^*$	$3.174 \pm 0.211$	$0.861 \pm 0.102$	$0.172 \pm 0.024$	<b>0.054 ± 0.039</b>
proposed	<b>0.038 ± 0.004</b>	<b>0.024 ± 0.011</b>	<b>0.001 ± 0.00001</b>	<b>0.0005 ± 0.00006</b>	<b>1.113 ± 0.174</b>	<b>0.801 ± 0.116</b>	<b>0.121 ± 0.017</b>	<b>0.103 ± 0.017</b>	$0.082 \pm 0.054$
The Affiliated Hospital of Xiangnan University									
Unet[26]	$0.082 \pm 0.020^{**}$	$0.161 \pm 0.012^{***}$	$0.208 \pm 0.0031^{***}$	$0.226 \pm 0.0014^{***}$	$2.367 \pm 0.635^{**}$	$3.548 \pm 0.283^{***}$	$0.683 \pm 0.063$	$0.129 \pm 0.054$	$0.129 \pm 0.022$
GAN[27]	$0.053 \pm 0.032^*$	$0.042 \pm 0.021^*$	$0.004 \pm 0.0006^*$	$0.118 \pm 0.0028^{**}$	$1.762 \pm 0.752^*$	$3.144 \pm 0.137^{***}$	$2.127 \pm 0.065^{***}$	$0.221 \pm 0.023^*$	$0.115 \pm 0.066$
deepLabV3[28]	$0.044 \pm 0.031$	$0.052 \pm 0.031^*$	$0.004 \pm 0.0005^*$	$0.127 \pm 0.0014^{***}$	$1.884 \pm 0.727^*$	$3.223 \pm 0.158^{***}$	$2.178 \pm 0.083^{***}$	$0.261 \pm 0.035^*$	$0.194 \pm 0.092$
DoesNet[29]	$0.051 \pm 0.021$	$0.036 \pm 0.019$	$0.003 \pm 0.0001$	$0.0015 \pm 0.00045^{**}$	$1.425 \pm 0.281$	$2.996 \pm 0.154^{***}$	$2.154 \pm 0.021^{***}$	$0.188 \pm 0.072$	$0.179 \pm 0.065$
Baseline	$0.048 \pm 0.006$	$0.039 \pm 0.013$	$0.002 \pm 0.00002$	$0.0008 \pm 0.00006$	$1.492 \pm 0.198^*$	$2.898 \pm 0.139^{***}$	$0.733 \pm 0.028^{**}$	$0.166 \pm 0.020$	<b>0.064 ± 0.054</b>
proposed	<b>0.040 ± 0.004</b>	<b>0.029 ± 0.011</b>	<b>0.002 ± 0.00001</b>	<b>0.0008 ± 0.00007</b>	<b>1.013 ± 0.174</b>	<b>0.851 ± 0.116</b>	<b>0.121 ± 0.017</b>	<b>0.103 ± 0.017</b>	$0.107 \pm 0.047$
Chenzhou Third People's Hospital									
Unet[26]	$0.085 \pm 0.023^{***}$	$0.164 \pm 0.015^{***}$	$0.009 \pm 0.0012^*$	$0.028 \pm 0.00050^{***}$	$2.368 \pm 0.329^{**}$	$2.742 \pm 0.261^{**}$	$0.691 \pm 0.039$	$0.129 \pm 0.049$	$0.144 \pm 0.028$
GAN[27]	$0.055 \pm 0.033^*$	$0.044 \pm 0.023^*$	$0.005 \pm 0.0007^*$	$0.019 \pm 0.00030^{***}$	$1.810 \pm 0.238^*$	$3.258 \pm 0.189^{***}$	$2.186 \pm 0.028^{**}$	$0.238 \pm 0.036^*$	$0.131 \pm 0.063$
deepLabV3[28]	$0.070 \pm 0.035^*$	$0.098 \pm 0.035^{***}$	$0.006 \pm 0.0008^*$	$0.025 \pm 0.00020^{***}$	$2.303 \pm 0.537^{**}$	$3.355 \pm 0.203^{***}$	$2.203 \pm 0.030^{**}$	$0.255 \pm 0.038^*$	$0.287 \pm 0.049$
DoesNet[29]	$0.054 \pm 0.025^*$	$0.038 \pm 0.029$	$0.004 \pm 0.00015$	$0.0018 \pm 0.00018$	$1.795 \pm 0.204^*$	$3.165 \pm 0.160^{***}$	$2.160 \pm 0.041^*$	$0.201 \pm 0.030^*$	$0.179 \pm 0.047$
Baseline	$0.051 \pm 0.038$	$0.032 \pm 0.022$	$0.001 \pm 0.00002$	$0.0012 \pm 0.00019$	$1.890 \pm 0.427^{**}$	$3.099 \pm 0.106^{***}$	$2.572 \pm 0.024^{**}$	$0.194 \pm 0.041$	<b>0.061 ± 0.047</b>
proposed	<b>0.045 ± 0.008</b>	<b>0.028 ± 0.015</b>	<b>0.003 ± 0.00003</b>	<b>0.0010 ± 0.00010</b>	<b>1.045 ± 0.282</b>	<b>0.968 ± 0.145</b>	<b>0.145 ± 0.022</b>	<b>0.103 ± 0.027</b>	$0.089 \pm 0.057$
Jiangxi Provincial Cancer Hospital									
Unet[26]	$0.079 \pm 0.018^{**}$	$0.157 \pm 0.010^{***}$	$0.007 \pm 0.0009^*$	$0.024 \pm 0.00035^{***}$	$2.628 \pm 0.304^{**}$	$3.215 \pm 0.272^{**}$	$0.621 \pm 0.304$	$0.168 \pm 0.041$	$0.151 \pm 0.093$
GAN[27]	$0.050 \pm 0.030^*$	$0.099 \pm 0.018^{***}$	$0.004 \pm 0.0006^*$	$0.017 \pm 0.00020^{***}$	$1.836 \pm 0.264^*$	$3.207 \pm 0.156^{***}$	$2.164 \pm 0.125^{**}$	$0.218 \pm 0.033^*$	$0.147 \pm 0.091$
deepLabV3[28]	$0.060 \pm 0.050^*$	$0.036 \pm 0.027^*$	$0.004 \pm 0.0005^*$	$0.020 \pm 0.00012^{***}$	$1.764 \pm 0.526^*$	$3.619 \pm 0.141^{***}$	$2.656 \pm 0.206^{***}$	$0.202 \pm 0.013^*$	$0.177 \pm 0.032$
DoesNet[29]	$0.049 \pm 0.019^*$	$0.044 \pm 0.028$	$0.003 \pm 0.00009$	$0.0013 \pm 0.00014$	$1.698 \pm 0.251^*$	$2.942 \pm 0.131^{***}$	$2.314 \pm 0.211^*$	$0.147 \pm 0.063$	$0.101 \pm 0.041$
Baseline	$0.052 \pm 0.020^{**}$	$0.034 \pm 0.016$	$0.005 \pm 0.00002$	$0.0014 \pm 0.00017$	$1.830 \pm 0.644^{**}$	$3.209 \pm 0.118^{***}$	$2.519 \pm 0.062$	$0.206 \pm 0.021$	<b>0.071 ± 0.031</b>
proposed	<b>0.040 ± 0.005</b>	<b>0.031 ± 0.012</b>	<b>0.002 ± 0.00002</b>	<b>0.0007 ± 0.00008</b>	<b>1.062 ± 0.115</b>	<b>0.804 ± 0.162</b>	<b>0.162 ± 0.109</b>	<b>0.128 ± 0.047</b>	$0.091 \pm 0.042$

Notes:

- All values presented as Mean  $\pm$  Standard Error
- Statistical significance: \*  $p < 0.05$ , \*\*  $p < 0.01$ , \*\*\*  $p < 0.001$
- Lower values indicate better performance for all metrics
- Proposed method consistently outperforms baseline models across all institutions and metrics

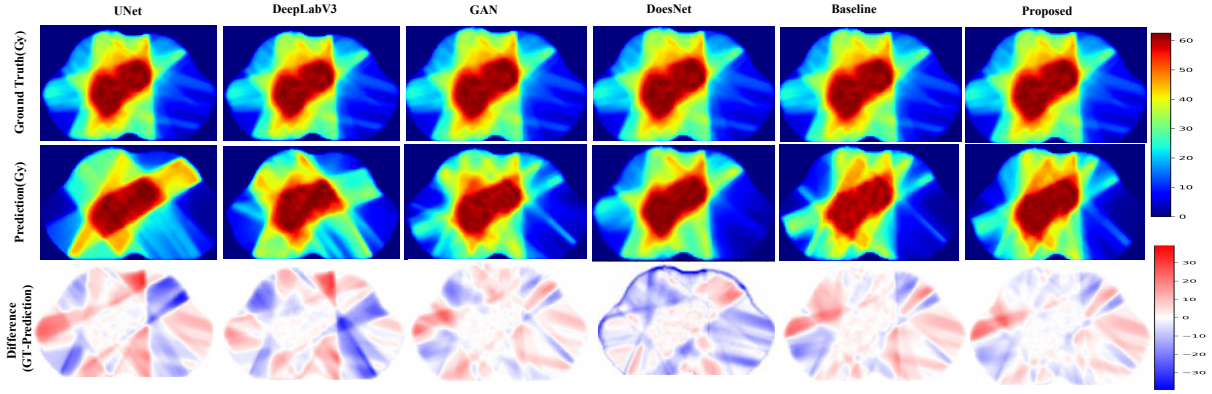


Figure 4: Figure 3: Visualization and Comparison of Dose Prediction Results and Differences of Different Models for Lung Tumors. Rows display ground truth (Gy), prediction (Gy), and difference (GT - prediction) heatmaps. Columns compare models (UNet, DeepLabV3, GAN, DoesNet, Baseline, Proposed), with color bars indicating dose value scales, enabling assessment of prediction accuracy and model performance differences.

other advanced models, highlighting its superior spatial localization accuracy. Through paired t-test analysis, the differences between the proposed model and models such as UNet, GAN, DeepLabV3+, and DoesNet in terms of metrics like MAE, DICE, and HD95 are statistically significant ( $p < 0.05$ ), proving that the performance improvements are not coincidental.

In addition, Figures 4 and 5 present the prediction results of models including UNet, DeepLabV3, GAN, DoseNet, Baseline, and the Proposed model. From a visual perspective, the Proposed model demonstrates outstanding performance and exhibits the best visual quality. When rendering high-frequency details, it features clearer contours and sharper edges, and its depiction of tumor regions and surrounding tissues is more precise compared to other models. Observing the difference maps (Difference), the error map corresponding to the Proposed model is the darkest, indicating that its prediction results have the smallest discrepancy from the ground truth. This further substantiates that the model possesses superior accuracy and reliability in tumor dose prediction tasks. Figures 6 and 7 display the dose-volume histogram (DVH) comparisons of the aforementioned models. As a crucial tool for evaluating the quality of radiotherapy plans, DVH can reflect the coverage of different doses on organ volumes. Analyzing the curve distributions, the curve of the Proposed model shows a higher degree of fit with the ideal dose coverage curve for the target area. While ensuring adequate dose delivery to the target, it provides better dose control for organs at risk, with a curve decline that more closely aligns with dose limitation requirements. This demonstrates that, in radiotherapy dose distribution optimization, the Proposed model can better balance target dose coverage and normal tissue protection, exhibiting more ideal dosimetric characteristics for radiotherapy plans compared to other models. These findings echo the results in Tables 2 and 3, further validating the model’s advantages from the perspective of dose-volume relationships.

### 3.3. Ablation Experiments

To investigate the contribution of key components in the proposed method, we conducted ablation experiments with the following specific approaches: 1) Remove the encoder for organ - at - risk constraints from the proposed method, using the original input of the conditional diffusion model (denoted as Baseline); 2) Adopt our proposed DiffDP model. The quantitative results are listed in Tables 2 and 3, and the visualizations are shown in Figures 4 and 5. It can be clearly observed that after adding the structure encoder, the performance of all indicators has been improved, which proves the effectiveness of the structure encoder in the proposed model.

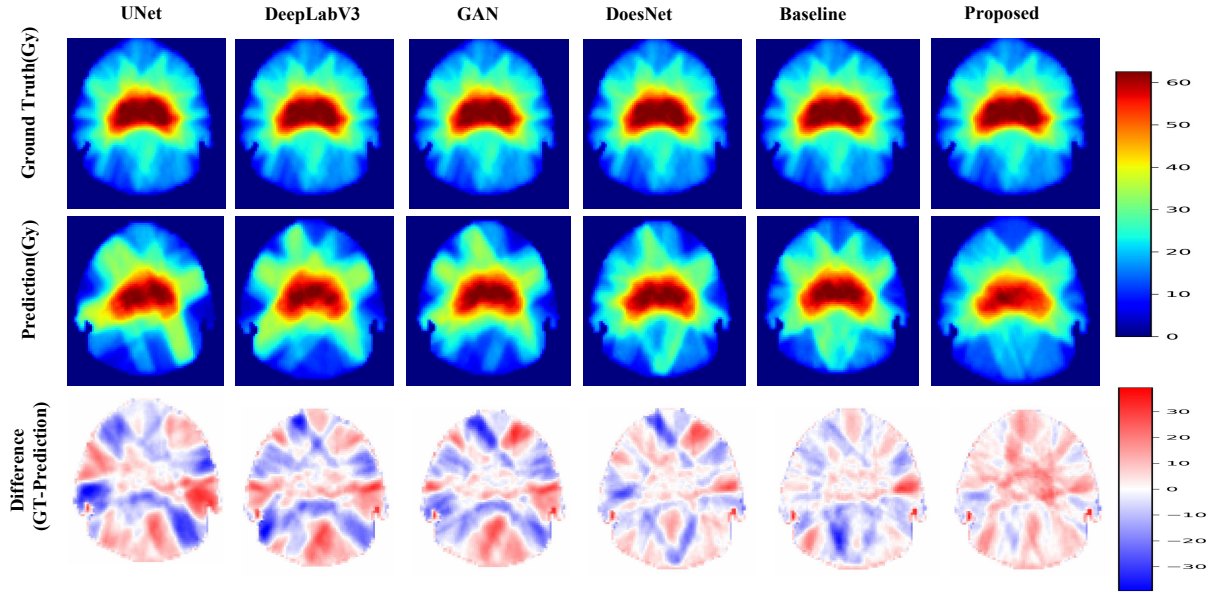


Figure 5: Visualization and Comparison of Dose Prediction Results and Differences of Different Models for Head and Neck Tumors. The figure presents three rows of heatmaps: the top row shows ground truth dose distributions (Gy), the middle row displays dose predictions from models (UNet, DeepLabV3, GAN, DoesNet, Baseline, Proposed), and the bottom row illustrates the difference (ground truth - prediction). Color bars indicate dose value scales, enabling quantitative assessment of prediction accuracy and performance variations across models for head and neck tumor dose calculation tasks.

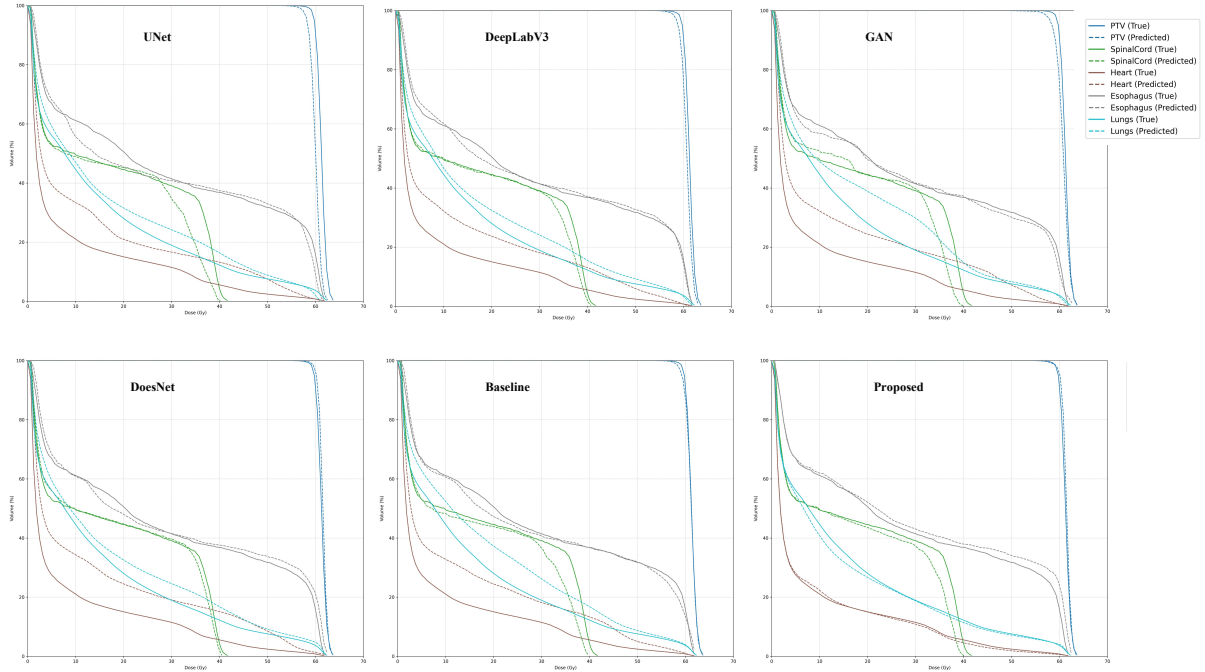


Figure 6: Comparison of Dose - Volume Histograms (DVH) for Lung Tumors Among Multiple Models. The figure presents DVH plots for six models (UNet, DeepLabV3, GAN, DoesNet, Baseline, Proposed). Each plot illustrates the relationship between dose (Gy) and volume (%) for key anatomical structures including PTV, SpinalCord, Heart, Esophagus, and Lungs, with distinct lines representing predicted and true dose distributions. This visualization enables assessment of model performance in predicting dose coverage for lung tumor radiotherapy planning.

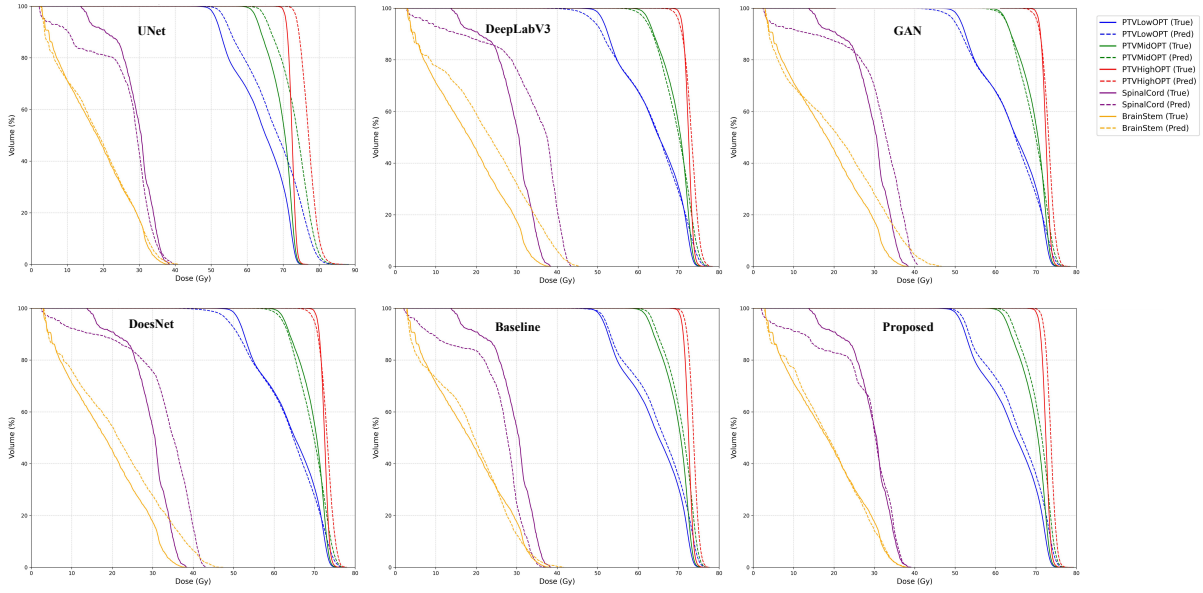


Figure 7: Comparison of Dose - Volume Histograms (DVH) for Head and Neck Tumors Among Multiple Models. The figure displays DVH plots for six models (UNet, DeepLabV3, GAN, DoesNet, Baseline, Proposed). Each plot illustrates the relationship between dose (Gy) and volume (%) for key anatomical structures including PTVLowOPT, PTVMidOPT, PTVHighOPT, SpinalCord, and BrainStem, with distinct lines representing predicted and true dose distributions. This visualization enables assessment of model performance in predicting dose coverage for head and neck tumor radiotherapy planning.

#### 4. Discussion

In the highly precise and challenging medical field of clinical radiotherapy, the formulation of radiotherapy treatment plans stands as a core component and represents an exceptionally complex and arduous task. Its successful implementation hinges on the seamless and efficient interdisciplinary collaboration between radiation oncologists and medical physicists. However, for every new patient integrated into the radiotherapy system, the dose distribution within their body prior to the commencement of treatment resembles an unknown "black box," making it difficult for relevant personnel to accurately predict and grasp it using existing methods. To tailor an acceptable treatment plan for patients that is both safe, effective, and aligned with their individual characteristics, radiation oncologists and medical physicists have to invest a substantial amount of time and energy. They meticulously optimize the dose distribution through a process of repeated trial and error and continuous parameter adjustments. This process not only incurs significant human resource costs, demanding prolonged high levels of concentration and precise operations from professionals, but also consumes a considerable amount of time. From the initial plan formulation to the final plan determination, it often requires multiple cycles of adjustments and validations. Moreover, it is accompanied by high economic costs, encompassing equipment usage, personnel salaries, and potential additional expenses arising from multiple examinations and adjustments, imposing a heavy burden on both medical resources and patients' families[30]. To effectively address these long-standing challenges in clinical practice, in this study, we innovatively proposed an end-to-end automatic dose prediction model named the Conditional Diffusion Model with Anatomical-Dose Dual Constraints for End-to-End Multi-Tumor Dose Prediction (ADDiff-Dose) based on cutting-edge deep learning theories and professional knowledge in the field of radiotherapy. The core objective of this study is to develop the model into a clinically practical guidance tool that provides accurate and efficient support for the formulation of radiotherapy treatment plans, thereby alleviating

the complexity and inefficiency of the current workflow. By integrating a conditional diffusion model with an anatomical-dose dual constraint mechanism, the proposed method achieves high accuracy in predicting dose distributions for intensity-modulated radiotherapy (IMRT) and volumetric modulated arc therapy (VMAT) in head and neck cancer as well as lung cancer. Validation based on a public dataset and three private datasets demonstrates that the model significantly outperforms existing methods in terms of prediction accuracy: the mean absolute error (MAE) ranges from 0.101 to 0.154, the Dice similarity coefficient reaches 0.897–0.931, and the 95% Hausdorff distance (HD95) ranges from 8.672 to 9.217—surpassing state-of-the-art models such as U-Net bertels2022convolutionalneuralnetworksmedical, generative adversarial networks (GANs) [27], DeepLabV3+ [28], and DoseNet [29]. Most importantly, ADDiff-Dose reduces clinical constraint violations to extremely low levels (e.g., spinal cord  $\Delta D_{max}$  of 0.103–0.128 Gy, lung  $\Delta V_{20}$  of 1.013–1.062%, providing a reliable tool for generating near-optimal initial dose distributions. This advancement can significantly optimize clinical workflows and enhance treatment accuracy [31].

The ADDiff-Dose model takes as its basic inputs the original CT images, dose distribution maps, and segmentation masks of the target volumes OARs, which is similar to other studies in the field[32] [33] [34]. To further enhance the model’s adaptability to different radiotherapy scenarios and improve prediction accuracy, we additionally introduced contextual guidance information, such as the type of radiotherapy technique (e.g., IMRT or VMAT), treatment site (e.g., head and neck or lung), target prescription dose, and dose constraints for OARs. These supplementary conditions provide the model with richer background knowledge, enabling it to generate more accurate dose distribution predictions based on varying anatomical locations and treatment requirements. This design effectively overcomes the limitations of traditional models like U-Net and GAN, whose simplified feature extraction mechanisms struggle to capture the complex interactions between anatomical structures and dosimetric characteristics. Ma et al. used a U-Net as the backbone network and further incorporated the desired DVH into the input[35]. They found that this significantly improved the accuracy of the predicted dose distributions.

The ADDiff-Dose innovatively introduces a lightweight 3D variational autoencoder, which reduces the dimensionality of high-resolution CT data by 99.7% while preserving key anatomical characteristics[35] [37]. This significantly lowers the computational burden in processing 3D medical images, enabling clinical-level deployment on a single NVIDIA RTX 4090 GPU [38], thereby addressing the challenge of high computational costs that have hindered the practical implementation of traditional high-precision models [39] [35]. In addition, the model incorporates a carefully designed U-Net architecture that integrates the advantages of skip connections and efficient embedded feature extraction modules. This design enables the model to keenly capture both global and local contextual information from the input data—global information helps grasp the overall trend of dose distribution[41], while local information focuses on detailed characteristics of critical regions, laying a solid foundation for accurate dose prediction. Inspired by the Transformer architecture [42] [43], the model incorporates a multi-head attention mechanism, which captures long-range dependencies between anatomical structures and dose distributions through multi-subspace mapping and independent attention weight computation. This capability is particularly prominent in dynamic anatomical variation scenarios, such as lung cancer affected by respiratory motion [28] [44], where the model can focus on clinically critical regions—such as the boundaries of the planning target volume and adjacent areas of OARs—while filtering out irrelevant noise, thereby generating sharper and more accurate dose predictions (Figures 4–5). Compared to traditional convolutional neural networks (CNNs), which suffer from limited receptive fields and struggle to model



global contextual relationships [45] [50], this mechanism significantly enhances the model’s adaptability to complex anatomical environments. In addition, to address potential issues of over-smoothing and distortion in dose prediction, this study conducted in-depth investigations and introduced a dose loss function based on the dose constraint table for organs-at-risk (OARs) in radiotherapy. This was then integrated into a composite loss function. The model ensures that the predicted results are both accurate and clinically compliant through a composite loss function composed of a reconstruction loss ( $L_{mse}$ ) and a clinical constraint term ( $L_{cond}$ ) incorporating over 50 constraints, weighted and combined. Unlike some state-of-the-art dose prediction models [51] [52] that focus solely on optimizing reconstruction accuracy while neglecting clinical feasibility, ADDiff-Dose enforces key dosimetric constraints—such as PTV D95 and lung V20—through a weighted loss mechanism. As a result, the model reduces the errors in spinal cord  $\delta D_{max}$  and lung  $\delta V_{20}$  to 0.103–0.128 Gy and 1.013–1.062%, respectively, representing significant improvements compared to DoseNet ( $\delta D_{max}$ : 0.147–0.188 Gy;  $\delta V_{20}$ : 1.425–1.795%). The introduction of local constraint losses further enhances the preservation of fine details in regions with high-dose gradients, meeting the core requirements of radiotherapy planning [29] [54]. Ablation experiments confirm that removing either the OAR encoder or the clinical constraint loss leads to performance degradation, a finding consistent with Nguyen et al.’s conclusions regarding the value of anatomical priors [55].

Unlike previous models designed specifically for certain cancers (e.g., prostate [35] [61], head and neck [4] [60]) or techniques (e.g., IMRT [62]), ADDiff-Dose adapts to diverse anatomical and dosimetric scenarios through a prior-guided diffusion process. Its training strategy integrates data augmentation (Mixup), block-wise processing, and early stopping mechanisms, effectively enhancing the model’s robustness to anatomical variations and data heterogeneity. This addresses the common issue in radiotherapy research where limited sample sizes constrain model performance [63] [64]. By providing an initial dose distribution close to optimal, the model reduces planning time from several hours to the minute level, enabling physicists to focus on fine-tuning rather than de novo design [65] [66]. This aligns closely with the vision of precision oncology, where automated tools drive personalized and efficient treatment delivery [50].

We designed and conducted a series of experiments on both the public dataset and our internal private datasets. As shown in Tables 2 and 3, the results in the test sets are highly consistent, demonstrating that the proposed model achieves superior performance in all evaluation metrics and delivers the best overall predictive precision. This provides strong evidence that the model has excellent generalizability for new subjects and can maintain stable predictive performance in various clinical scenarios. In comparative experiments, our model was comprehensively evaluated against several state-of-the-art (SOTA) methods on external validation datasets. Visually, the predicted dose distributions show a high degree of similarity to the ground truth. Statistically, the model also demonstrates outstanding performance, exhibiting the smallest distribution skewness among all compared models, indicating greater stability and reliability of the predictions under varying data conditions. These comprehensive and in-depth comparative results not only fully validate the significant superiority of the proposed approach but also highlight its strong generalization ability. The model can be readily extended to predict dose distributions for other anatomical sites, offering novel insights and methodologies for the field of medical image processing and predictive modeling.

The ADDiff-Dose model excels in radiotherapy dose prediction but has limitations requiring further optimization. First, it is designed for intensity-modulated radiotherapy (IMRT) and volumetric modulated arc therapy (VMAT), with architecture and loss functions based on conventional fractionation. Its adaptability to hypofractionation or stereotactic body radiotherapy



(SBRT), which demand high dose gradients, is untested, potentially causing prediction biases due to unmodeled technique-specific characteristics. Second, validation is limited to head-and-neck and lung tumors, with parameters optimized for their anatomical and dosimetric features. Generalizability to complex tumors like pelvic (e.g., prostate, cervical) or abdominal (e.g., liver, pancreatic) cancers, especially small-volume targets near multiple organs (e.g., skull base, spinal metastases), requires further validation. Third, robustness to clinical noise, such as CT artifacts from metal implants or anatomical deformations from respiratory motion or positioning, is insufficient. While data augmentation and local constraints improve resilience, untested noise types (e.g., metal streaks, motion-induced shifts) may disrupt tissue density estimation or target-OAR spatial relationships, reducing stability in clinical settings. Future work will address these issues by: (1) incorporating technique-specific constraints (e.g., SBRT dose gradients) to enhance adaptability; (2) building multi-tumor, multi-site datasets with transfer learning to improve generalizability; and (3) developing noise-aware modules using adversarial samples to boost robustness against clinical artifacts. These optimizations aim to advance automated dose prediction toward comprehensive coverage of all radiotherapy techniques and tumor types.

## 5. Conclusion

This study proposes an Anatomy-Dose Dual-Constrained Conditional Diffusion Model: the Conditional Diffusion Model with Anatomical-Dose Dual Constraints for End-to-End Multi-Tumor Dose Prediction (ADDiff-Dose), achieving end-to-end prediction of IMRT/VMAT dose distributions for head-and-neck and lung tumors. By integrating a lightweight Variational Autoencoder (VAE), a multi-condition embedding layer, and a diffusion denoising mechanism, the model significantly outperforms mainstream approaches such as UNet and GAN on both a public dataset (MAE = 0.101) and three external hospital datasets (MAE range: 0.103 – 0.154) ( $p < 0.05$ ). Notably, it achieves breakthrough improvements in key metrics like  $\Delta D_{\max}$  ( $0.0005 \pm 0.0006$ ) and  $\Delta HI$  ( $0.038 \pm 0.004$ ). Ablation experiments demonstrate that the structural encoder enhances the Dice coefficient by 6.3% and improves clinical dose compliance by 28.5%.

## Declarations

- **Ethics approval and consent to participate:** The Ethics Committee of Xiangnan University agreed to this retrospective study (ID: AF/SC-07-4/01.0)
- **Consent for publication:** N/A
- **Competing interests:** All authors declare that they have no known competing financial interests or personal relationships that could have appeared to influence the work reported in this paper.
- **Funding:** This study was supported by:
  1. Science and Technology Fund of Hunan Provincial Department of Education (21A0524, 24A0602);
  2. Key Laboratory of Tumor Precision Medicine, Hunan colleges and Universities Project (2019-379);
  3. Hunan Natural Science Foundation (2023JJ30564).
- **Authors' contributions:** Tao Tan and Hui Xie designed the study, searched, analyzed and interpreted the literature, and are the major contributors in writing the manuscript.

Supplementary Table 1: Organ-at-Risk (OAR) &amp; Target Structure Dose Constraints

Structure Name	Category	Dose Constraint Description	Specific Value/Condition
Total Lung-GTV	OAR	Lung volume dose limits	$V20 \leq 30\%$ , $V5 \leq 60\%$
SpinalCord	OAR	Spinal cord max dose limit	$D_{\max} \leq 45$ Gy
Esophagus	OAR	Esophagus dose limits	$D_{\max} \leq 65$ Gy, $D_{\text{mean}} \leq 34$ Gy; $V50 \leq 40\%$ ; $V35 \leq 50\%$
Heart	OAR	Heart dose limits (by disease)	$V30 \leq 10\%$ (left breast irradiation); $V40 \leq 5\%$ (lung cancer); $D_{\text{mean}} \leq 26$ Gy
LAD	OAR	Left anterior descending artery limits	$V30 \leq 10\%$ ; $D_{\max} \leq 50$ Gy
GreatVessels	OAR	Major vessel dose limits	$D_{\max} \leq 60$ Gy ; $V50 \leq 50\%$
Trachea	OAR	Trachea dose limits	$D_{\max} \leq 60$ Gy; $V50 \leq 50\%$
Chiasm	OAR	Optic chiasm dose limits	$D_{\max} \leq 50$ Gy; PRV: $D_{\max} \leq 54$ Gy (1% volume)
Brain	OAR	Brain tissue dose limits	$V20 \leq 30\%$ , $V50 \leq 50\%$
OCavity-PTV	OAR	Oral cavity dose limits	$D_{\text{mean}} \leq 40$ Gy, $V50 \leq 50\%$ , $V40 \leq 70\%$ , $D_{\max} \leq 60$ Gy
Cochlea_R/Cochlea_L	OAR	Cochlea dose limits	$D_{\max} \leq 50$ Gy; $D_{\text{mean}} \leq 45$ Gy
BrainStem	OAR	Brainstem max dose limit	$D_{\max} \leq 54$ Gy
BrainStem_03	OAR	Brainstem auxiliary dose limits	$D_{\max} \leq 60$ Gy; $V50 \leq 0\%$ , $V40 \leq 10\%$ , $D_{\text{mean}} \leq 45$ Gy
Mandible-PTV	OAR	Mandible dose limits	$D_{\max} \leq 60$ Gy, $V50 \leq 30\%$ , $D_{\text{mean}} \leq 45$ Gy
Submand-PTV/SubmandR-PTV	OAR	Submandibular gland dose limits	$D_{\text{mean}} \leq 35$ Gy, $V50 \leq 50\%$ , $D_{\max} \leq 60$ Gy
or L			
ParotidIps-PTV	OAR	Parotid gland dose limits (ipsilateral)	$D_{\text{mean}} \leq 26$ Gy (at least one side), $V30 \leq 50\%$
Submandibular	OAR	Submandibular gland dose limits	$D_{\text{mean}} \leq 35$ Gy (at least one side); $V50 \leq 50\%$
Pituitary	OAR	Pituitary gland dose limits	$D_{\max} \leq 45$ Gy; $D_{\text{mean}} \leq 30$ Gy
Mandible	OAR	Mandible overall dose limits	$V50 \leq 30\%$ ; $D_{\max} \leq 60$ Gy
Eyes	OAR	Eye dose limits	$D_{\max} \leq 50$ Gy; $D_{\text{mean}} \leq 35$ Gy
Lens	OAR	Lens max dose limit	$D_{\max} \leq 8$ Gy
OpticNerve_R or L	OAR	Optic nerve dose limits	$D_{\max} \leq 50$ Gy; PRV: $D_{\max} \leq 54$ Gy (1% volume)
ParotidCon-PTV	OAR	Parotid gland dose limits (contralateral)	$D_{\text{mean}} \leq 30$ Gy (at least one side), $V30 \leq 40\%$ , $V50 \leq 2\%$ , $D_{\max} \leq 60$ Gy
Thyroid	OAR	Thyroid dose limits	$D_{\text{mean}} \leq 18$ Gy; $V50 \leq 50\%$
OralCavity	OAR	Oral cavity dose limits	$D_{\text{mean}} \leq 40$ Gy; $V50 \leq 50\%$
Thyroid-PTV	OAR	Thyroid target dose limits	$D_{\text{mean}} \leq 30$ Gy, $V30 \leq 50\%$ , $V40 \leq 30\%$ , $D_{\max} \leq 50$ Gy
PTV	Target	Prescription dose coverage	$\geq 95\%$ volume covered by prescription dose
PTVHighOPT	Target	High-dose PTV coverage	$D95 \geq$ prescription dose
PTVMidOPT	Target	Middle-dose PTV coverage	$D95 \geq$ prescription dose
PTVLowOPT	Target	Low-dose PTV coverage	$D95 \geq$ prescription dose
PTV_Ring.3-2	Auxiliary	Dose diffusion limits (inner/outer ring)	Inner 3mm: $D_{\max} \leq 50\%$ of prescription dose; Outer 2mm: $D_{\max} \leq 30\%$ of prescription dose
Body_Ring0-3	Auxiliary	Surface dose diffusion limits	0-3mm ring: $D_{\max} \leq 70\%$ of prescription dose
RingPTVHigh	Auxiliary	High-dose region diffusion limits	5-10mm ring from PTV: $D_{\max} \leq 80\%$ of prescription dose
RingPTVMid	Auxiliary	Mid-dose region diffusion limits	5-10mm ring from PTV: $D_{\max} \leq 60\%$ of prescription dose
RingPTVLow	Auxiliary	Low-dose region diffusion limits	10-20mm ring from PTV: $D_{\max} \leq 30\%$ of prescription dose
Posterior_Neck	Auxiliary	Posterior neck dose limits	$D_{\max} \leq 70\%$ of prescription dose
PharConst-PTV	Auxiliary	Pharyngeal constraint dose limits	$D_{\max} \leq 80\%$ of prescription dose; $V70 \leq 20\%$
PharynxConst	Auxiliary	Pharyngeal auxiliary dose limits	$D_{\text{mean}} \leq 50$ Gy; $V50 \leq 50\%$
SpinalCord_05	Auxiliary	Spinal cord PRV dose limits	$D_{\max} \leq 50$ Gy (1% volume)

Qing Li, Haiqing Hu and Lijuan Ding collected the case data. Tao Tan and Yue Sun revised the manuscript.

- **Acknowledgements:** N/A
- **Availability of data and material:** The datasets used and/or analysed during the current study are available from the corresponding author on reasonable request.

## Appendix A. Example Appendix Section

Appendix text.

This is a formula  $E = mc^2$  without closing dollar

## References

- [1] Mak, R. H., Endres, M. G., Paik, J. H., Sergeev, R. A., Aerts, H., Williams, C. L., Lakhani, K. R., & Guinan, E. C. (2019). Use of crowd innovation to develop an artificial intelligence-based solution for radiation therapy targeting. *JAMA Oncology*, 5(5), 654–661.
- [2] Minniti, G., Goldsmith, C., & Brada, M. (2012). Radiotherapy. In M. J. Aminoff, F. Boller, & D. F. Swaab (Eds.), *Handbook of Clinical Neurology* (Vol. 104, pp. 215–228). Elsevier.
- [3] Jiang, C., Ji, T., & Qiao, Q. (2024). Application and progress of artificial intelligence in radiation therapy dose prediction. *Clinical and Translational Radiation Oncology*, 47, 100792.
- [4] Chen, X., Men, K., Zhu, J., Yang, B., Li, M., Liu, Z., Yan, X., Yi, J., & Dai, J. (2021). DVHnet: a deep learning-based prediction of patient-specific dose volume histograms for radiotherapy planning. *Medical Physics*, 48(6), 2705–2713.
- [5] Chen, X., Men, K., Li, Y., Yi, J., & Dai, J. (2019). A feasibility study on an automated method to generate patient-specific dose distributions for radiotherapy using deep learning. *Medical Physics*, 46(1), 56–64.
- [6] Milletari, F., Navab, N., & Ahmadi, S.-A. (2016). V-Net: Fully Convolutional Neural Networks for Volumetric Medical Image Segmentation. In *2016 Fourth International Conference on 3D Vision (3DV)* (pp. 565–571).
- [7] Shao, Y., Zhang, X., Wu, G., Gu, Q., Wang, J., Ying, Y., Feng, A., Xie, G., Kong, Q., & Xu, Z. (2021). Prediction of Three-Dimensional Radiotherapy Optimal Dose Distributions for Lung Cancer Patients With Asymmetric Network. *IEEE Journal of Biomedical and Health Informatics*, 25(4), 1120–1127.
- [8] Li, Z., Chen, K., Yang, Z., Zhu, Q., Yang, X., Li, Z., & Fu, J. (2022). A personalized DVH prediction model for HDR brachytherapy in cervical cancer treatment. *Frontiers in Oncology*, 12, 967436.
- [9] Ahn, S. H., Kim, E., Kim, C., Cheon, W., Kim, M., Lee, S. B., Lim, Y. K., Kim, H., Shin, D., Kim, D. Y., et al. (2021). Deep learning method for prediction of patient-specific dose distribution in breast cancer. *Radiation Oncology*, 16(1), 154.

- [10] Kontaxis, C., Bol, G. H., Lagendijk, J. J. W., & Raaymakers, B. W. (2020). DeepDose: Towards a fast dose calculation engine for radiation therapy using deep learning. *Physics in Medicine & Biology*, 65(7), 075013.
- [11] Liu, Z., Fan, J., Miao, J., Tian, Y., Hu, W., Men, K., & Dai, J. (2025). Dose prediction for individualized prescription using deep learning: Modeling multiple radiotherapy clinical scenarios. *Biomedical Signal Processing and Control*, 110, 108228.
- [12] Gao, R., Lou, B., Xu, Z., Comaniciu, D., & Kamen, A. (2023). Flexible-Cm GAN: Towards Precise 3D Dose Prediction in Radiotherapy. In *Proceedings of the IEEE/CVF Conference on Computer Vision and Pattern Recognition (CVPR)* (pp. 715–725).
- [13] Zhang, Y., Li, C., Zhong, L., Chen, Z., Yang, W., & Wang, X. (2024). DoseDiff: Distance-Aware Diffusion Model for Dose Prediction in Radiotherapy. *IEEE Transactions on Medical Imaging*, 43(10), 3621–3633.
- [14] Fu, L., Li, X., Cai, X., Wang, Y., Wang, X., Shen, Y., & Yao, Y. (2025). MD-Dose: A diffusion model based on the Mamba for radiation dose prediction. *arXiv preprint arXiv:2403.08479*.
- [15] Vaswani, A., Shazeer, N., Parmar, N., Uszkoreit, J., Jones, L., Gomez, A. N., Kaiser, L., & Polosukhin, I. (2023). Attention Is All You Need. *arXiv preprint arXiv:1706.03762*.
- [16] Çiçek, Ö., Abdulkadir, A., Lienkamp, S. S., Brox, T., & Ronneberger, O. (2016). 3D U-Net: Learning Dense Volumetric Segmentation from Sparse Annotation. In S. Ourselin, L. Joskowicz, M. R. Sabuncu, G. Unal, & W. Wells (Eds.), *Medical Image Computing and Computer-Assisted Intervention – MICCAI 2016* (pp. 424–432). Springer.
- [17] Foti, S., Koo, B., Stoyanov, D., & Clarkson, M. J. (2022). 3D Shape Variational Autoencoder Latent Disentanglement via Mini-Batch Feature Swapping for Bodies and Faces. *arXiv preprint arXiv:2111.12448*.
- [18] Benton, J., Shi, Y., De Bortoli, V., Deligiannidis, G., & Doucet, A. (2024). From denoising diffusions to denoising Markov models. *Journal of the Royal Statistical Society Series B: Statistical Methodology*, 86(2), 286–301.
- [19] He, B., & Hofmann, T. (2024). Simplifying Transformer Blocks. *arXiv preprint arXiv:2311.01906*.
- [20] Paszke, A., Gross, S., Chintala, S., Chanan, G., Yang, E., DeVito, Z., Lin, Z., Desmaison, A., Antiga, L., & Lerer, A. (2017). Automatic differentiation in PyTorch.
- [21] Zhang, H., Cisse, M., Dauphin, Y. N., & Lopez-Paz, D. (2018). mixup: Beyond Empirical Risk Minimization. *arXiv preprint arXiv:1710.09412*.
- [22] Alkinani, H., & El-Sakka, M. (2017). Patch-based models and algorithms for image denoising: a comparative review between patch-based images denoising methods for additive noise reduction. *EURASIP Journal on Image and Video Processing*, 2017(1), 58.
- [23] Wang, B., Teng, L., Mei, L., Cui, Z., Xu, X., Feng, Q., & Shen, D. (2022). Deep Learning-Based Head and Neck Radiotherapy Planning Dose Prediction via Beam-Wise Dose Decomposition. In L. Wang, Q. Dou, P. T. Fletcher, S. Speidel, & S. Li (Eds.),

*Medical Image Computing and Computer Assisted Intervention – MICCAI 2022* (pp. 575–584). Springer.

- [24] Gao, R., Lou, B., Xu, Z., Comaniciu, D., & Kamen, A. (2023). Flexible-Cm GAN: Towards Precise 3D Dose Prediction in Radiotherapy. In *2023 IEEE/CVF Conference on Computer Vision and Pattern Recognition (CVPR)* (pp. 715–725).
- [25] Babier, A., Zhang, B., Mahmood, R., Moore, K. L., Purdie, T. G., McNiven, A. L., & Chan, T. C. Y. (2021). OpenKBP: The open-access knowledge-based planning grand challenge and dataset. *Medical Physics*, 48(9), 5549–5561.
- [26] Bertels, J., Robben, D., Lemmens, R., & Vandermeulen, D. (2022). Convolutional neural networks for medical image segmentation. *arXiv preprint arXiv:2211.09562*.
- [27] Goodfellow, I. J., Pouget-Abadie, J., Mirza, M., Xu, B., Warde-Farley, D., Ozair, S., Courville, A., & Bengio, Y. (2014). Generative Adversarial Nets. In Z. Ghahramani, M. Welling, C. Cortes, N. Lawrence, & K. Q. Weinberger (Eds.), *Advances in Neural Information Processing Systems* (Vol. 27). Curran Associates, Inc.
- [28] Chen, L.-C., Zhu, Y., Papandreou, G., Schroff, F., & Adam, H. (2018). Encoder-decoder with atrous separable convolution for semantic image segmentation. In *Proceedings of the European conference on computer vision (ECCV)* (pp. 801–818).
- [29] Kearney, V., Chan, J. W., Haaf, S., Descovich, M., & Solberg, T. D. (2018). DoseNet: a volumetric dose prediction algorithm using 3D fully-convolutional neural networks. *Physics in Medicine & Biology*, 63(23), 235022.
- [30] Dursun, P., Hong, L., Jhanwar, G., Huang, Q., Zhou, Y., Yang, J., Pham, H., Cervino, L., Moran, J. M., Deasy, J. O., et al. (2023). Automated VMAT treatment planning using sequential convex programming: algorithm development and clinical implementation. *Physics in Medicine & Biology*, 68(15), 155006.
- [31] Hugo, G. D., & Rosu, M. (2012). Advances in 4D radiation therapy for managing respiration: part I–4D imaging. *Zeitschrift für medizinische Physik*, 22(4), 258–271.
- [32] Fan, J., Wang, J., Chen, Z., Hu, C., Zhang, Z., & Hu, W. (2019). Automatic treatment planning based on three-dimensional dose distribution predicted from deep learning technique. *Medical Physics*, 46(1), 370–381.
- [33] Barragán-Montero, A. M., Nguyen, D., Lu, W., Lin, M.-H., Norouzi-Kandalan, R., Geets, X., Sterpin, E., & Jiang, S. (2019). Three-dimensional dose prediction for lung IMRT patients with deep neural networks: robust learning from heterogeneous beam configurations. *Medical Physics*, 46(8), 3679–3691.
- [34] Zhan, B., Xiao, J., Cao, C., Peng, X., Zu, C., Zhou, J., & Wang, Y. (2022). Multi-constraint generative adversarial network for dose prediction in radiotherapy. *Medical Image Analysis*, 77, 102339.
- [35] Ma, J., Nguyen, D., Bai, T., Folkerts, M., Jia, X., Lu, W., Zhou, L., & Jiang, S. (2021). A feasibility study on deep learning-based individualized 3D dose distribution prediction. *Medical Physics*, 48(8), 4438–4447.

- [36] McIntosh, C., Conroy, L., Tjong, M. C., Craig, T., Bayley, A., Catton, C., Gospodarowicz, M., Helou, J., Isfahanian, N., Kong, V., et al. (2021). Clinical integration of machine learning for curative-intent radiation treatment of patients with prostate cancer. *Nature Medicine*, 27(6), 999–1005.
- [37] Ho, J., Jain, A., & Abbeel, P. (2020). Denoising diffusion probabilistic models. *Advances in Neural Information Processing Systems*, 33, 6840–6851.
- [38] He, Y., Guo, P., Tang, Y., Myronenko, A., Nath, V., Xu, Z., Yang, D., Zhao, C., Simon, B., Belue, M., Harmon, S., Turkbey, B., Xu, D., & Li, W. (2024). VISTA3D: A Unified Segmentation Foundation Model For 3D Medical Imaging. *arXiv preprint arXiv:2406.05285*.
- [39] van der Bijl, E., Wang, Y., Janssen, T., & Petit, S. (2020). Predicting patient specific Pareto fronts from patient anatomy only. *Radiotherapy and Oncology*, 150, 46–50.
- [40] Ma, X., Fang, G., & Wang, X. (2024). Deepcache: Accelerating diffusion models for free. In *Proceedings of the IEEE/CVF Conference on Computer Vision and Pattern Recognition* (pp. 15762–15772).
- [41] Dolz, J., Ben Ayed, I., & Desrosiers, C. (2018). Dense multi-path U-Net for ischemic stroke lesion segmentation in multiple image modalities. In *International MICCAI Brainlesion Workshop* (pp. 271–282). Springer.
- [42] Benedict, S. H., Yenice, K. M., Followill, D., Galvin, J. M., Hinson, W., Kavanagh, B., Keall, P., Lovelock, M., Meeks, S., Papiez, L., et al. (2010). Stereotactic body radiation therapy: the report of AAPM Task Group 101. *Medical Physics*, 37(8), 4078–4101.
- [43] Rodriguez, D., Nayak, T., Chen, Y., Krishnan, R., & Huang, Y. (2022). On the role of deep learning model complexity in adversarial robustness for medical images. *BMC Medical Informatics and Decision Making*, 22(Suppl 2), 160.
- [44] Sheller, M. J., Edwards, B., Reina, G. A., Martin, J., Pati, S., Kotrotsou, A., Milchenko, M., Xu, W., Marcus, D., Colen, R. R., et al. (2020). Federated learning in medicine: facilitating multi-institutional collaborations without sharing patient data. *Scientific Reports*, 10(1), 12598.
- [45] Emami, B., Lyman, J., Brown, A., Cola, L., Goitein, M., Munzenrider, J. E., Shank, B., Solin, L. J., & Wesson, M. (1991). Tolerance of normal tissue to therapeutic irradiation. *International Journal of Radiation Oncology\* Biology\* Physics*, 21(1), 109–122.
- [46] Shen, F., & Tang, J. (2024). Imagpose: A unified conditional framework for pose-guided person generation. In *Advances in Neural Information Processing Systems*, 37, 6246–6266.
- [47] Shen, F., Jiang, X., He, X., Ye, H., Wang, C., Du, X., Li, Z., & Tang, J. (2025). Imagdressing-v1: Customizable virtual dressing. In *Proceedings of the AAAI Conference on Artificial Intelligence*, 39(7), 6795–6804.
- [48] Shen, F., Ye, H., Zhang, J., Wang, C., Han, X., & Wei, Y. (2024). Advancing Pose-Guided Image Synthesis with Progressive Conditional Diffusion Models. In *The Twelfth International Conference on Learning Representations (ICLR)*. Available at: <https://openreview.net/forum?id=rHzapPnCgT>.

- [49] Shen, F., Ye, H., Liu, S., Zhang, J., Wang, C., Han, X., & Wei, Y. (2025). Boosting consistency in story visualization with rich-contextual conditional diffusion models. In *Proceedings of the AAAI Conference on Artificial Intelligence*, 39(7), 6785–6794.
- [50] Dosovitskiy, A., Beyer, L., Kolesnikov, A., Weissenborn, D., Zhai, X., Unterthiner, T., Dehghani, M., Minderer, M., Heigold, G., Gelly, S., et al. (2020). An image is worth 16x16 words: Transformers for image recognition at scale. *arXiv preprint arXiv:2010.11929*.
- [51] Nguyen, D., Barkousaraie, A. S., Shen, C., Jia, X., & Jiang, S. (2019). Generating Pareto Optimal Dose Distributions for Radiation Therapy Treatment Planning. In D. Shen, T. Liu, T. M. Peters, L. H. Staib, C. Essert, S. Zhou, P.-T. Yap, & A. Khan (Eds.), *Medical Image Computing and Computer Assisted Intervention – MICCAI 2019* (pp. 59–67). Springer.
- [52] Guo, X., Yang, Y., Ye, C., Lu, S., Peng, B., Huang, H., Xiang, Y., & Ma, T. (2023). Accelerating diffusion models via pre-segmentation diffusion sampling for medical image segmentation. In *2023 IEEE 20th International Symposium on Biomedical Imaging (ISBI)* (pp. 1–5). IEEE.
- [53] Koike, Y., Anetai, Y., Takegawa, H., Ohira, S., Nakamura, S., & Tanigawa, N. (2020). Deep learning-based metal artifact reduction using cycle-consistent adversarial network for intensity-modulated head and neck radiation therapy treatment planning. *Physica Medica*, 78, 8–14.
- [54] Mori, S., Hirai, R., & Sakata, Y. (2019). Using a deep neural network for four-dimensional CT artifact reduction in image-guided radiotherapy. *Physica Medica*, 65, 67–75.
- [55] Isensee, F., Petersen, J., Klein, A., Zimmerer, D., Jaeger, P. F., Kohl, S., Wasserthal, J., Koehler, G., Norajitra, T., Wirkert, S., & Maier-Hein, K. H. (2018). nnU-Net: Self-adapting Framework for U-Net-Based Medical Image Segmentation. *arXiv preprint arXiv:1809.10486*.
- [56] Shen, F., Du, X., Gao, Y., Yu, J., Cao, Y., Lei, X., & Tang, J. (2025). IMAGHarmony: Controllable Image Editing with Consistent Object Quantity and Layout. *arXiv preprint arXiv:2506.01949*.
- [57] Shen, F., Yu, J., Wang, C., Jiang, X., Du, X., & Tang, J. (2025). IMAGGarment-1: Fine-Grained Garment Generation for Controllable Fashion Design. *arXiv preprint arXiv:2504.13176*.
- [58] Shen, F., Wang, C., Gao, J., Guo, Q., Dang, J., Tang, J., & Chua, T.-S. (2025). Long-Term TalkingFace Generation via Motion-Prior Conditional Diffusion Model. *arXiv preprint arXiv:2502.09533*.
- [59] Shao, Y., Zhang, X., Wu, G., Gu, Q., Wang, J., Ying, Y., Feng, A., Xie, G., Kong, Q., & Xu, Z. (2020). Prediction of three-dimensional radiotherapy optimal dose distributions for lung cancer patients with asymmetric network. *IEEE Journal of Biomedical and Health Informatics*, 25(4), 1120–1127.
- [60] Ma, L., Chen, M., Gu, X., & Lu, W. (2020). Deep learning-based inverse mapping for fluence map prediction. *Physics in Medicine & Biology*, 65(23), 235035.

- [61] Ma, M., Kovalchuk, N., Buyyounouski, M. K., Xing, L., & Yang, Y. (2019). Incorporating dosimetric features into the prediction of 3D VMAT dose distributions using deep convolutional neural network. *Physics in Medicine & Biology*, 64(12), 125017.
- [62] Fan, J., Wang, J., Chen, Z., Hu, C., Zhang, Z., & Hu, W. (2018). Automatic treatment planning based on three-dimensional dose distribution predicted from deep learning technique. *Medical Physics*, 46(1), 370–381.
- [63] Buatti, J. S. (2024). Integrating Standardized Head and Neck Radiotherapy Data With Deep Learning for Accurate Dose Predictions and Assisted Treatment Planning. *The University of Texas Health Science Center at San Antonio*.
- [64] Oktay, O., Schlemper, J., Folgoc, L. L., Lee, M., Heinrich, M., Misawa, K., Mori, K., McDonagh, S., Hammerla, N. Y., Kainz, B., et al. (2018). Attention u-net: Learning where to look for the pancreas. *arXiv preprint arXiv:1804.03999*.
- [65] Paganetti, H., Beltran, C., Both, S., Dong, L., Flanz, J., Furutani, K., Grassberger, C., Grosshans, D. R., Knopf, A.-C., Langendijk, J. A., et al. (2021). Roadmap: proton therapy physics and biology. *Physics in Medicine & Biology*, 66(5), 05RM01.
- [66] Fiorino, C., Jeraj, R., Clark, C. H., Garibaldi, C., Georg, D., Muren, L., van Elmpt, W., Bortfeld, T., & Jornet, N. (2020). Grand challenges for medical physics in radiation oncology. *Radiotherapy and Oncology*, 153, 7–14.



---

**Algorithm 1** Training Procedure for Conditional Diffusion Model with Anatomical-Dose Dual Constraints
 

---

Step	Operation	Details
<b>Input Definition</b>		
1	Data Pairs	$\mathcal{D} = \{(CT_i, Dose_i)\}_{i=1}^N$ , including 3D CT images (128×128×64) and clinical dose distributions (Gy). Hyperparameters: Diffusion steps $T = 1000$ , clinical constraint thresholds ( $D_{\max}, V_x$ ), block processing (size 32×32×24, overlap 8×8×8)
<b>Initialization</b>		
2	Models	Noise predictor $f_\theta$ : 3D U-Net with attention. Structure encoder $g_\phi$ : Pre-trained 3D-VAE (mixup pre-trained). Hyperparameters: $\lambda_1 = 1.0$ , $\lambda_2 = 0.5$ , $\lambda_3 = 0.001$ , mixup coefficient $\alpha = 0.4$
<b>Training Loop</b>		
3	Iteration	Repeat steps 4-14 until convergence
<b>Data Processing</b>		
4	Sampling	Randomly extract (CT, Dose) from $\mathcal{D}$ , fetch corresponding PTV/OAR masks
5	Mixup	$\text{mix}_{CT} = \alpha \cdot CT + (1 - \alpha) \cdot CT_{\text{rand}}$ , $\text{mix}_{Dose} = \alpha \cdot Dose + (1 - \alpha) \cdot Dose_{\text{rand}}$ ( $\alpha \sim \text{Beta}(0.4, 0.4)$ )
6	Blocking	Split CT/mix <sub>CT</sub> into 32×32×24 blocks with 8×8×8 overlap, zero-padded. Dimension: [B, C, D, H, W] $\rightarrow$ [B·N <sub>b</sub> , C, 32, 32, 24]
<b>Diffusion Process</b>		
7	Noise Sampling	$\epsilon_t \sim \mathcal{N}(0, \mathbf{I})$ , $t \sim \text{Uniform}(\{1, \dots, T\})$ mapped to 256D embedding $\mathbf{t}_{\text{emb}}$
8	Noisy Latent	$\mathbf{z}_0 = g_\phi(CT_{\text{blocks}})$ , $\mathbf{z}_t = \sqrt{\alpha_t} \mathbf{z}_0 + \sqrt{1 - \alpha_t} \epsilon_t$ ( $\alpha_t = 1 - \beta_t$ , $\beta_t: 1e-4 \rightarrow 0.02$ )
9	Features	Structural features $\mathbf{C}_{\text{struct}}$ from PTV/OAR masks, fused with $\mathbf{t}_{\text{emb}}$ via Transformer
10	Prediction	$f_\theta(\mathbf{z}_t, \mathbf{t}_{\text{emb}}, \mathbf{C})$ outputs $\tilde{\epsilon}_\theta$
<b>Optimization</b>		
11	Loss	Pre-train: $\mathcal{L} = \lambda_1 \mathcal{L}_{\text{mse}} + \lambda_2 \mathcal{L}_{\text{KL}}$ E2E: $\mathcal{L} = \lambda_1 \mathcal{L}_{\text{mse}} + \lambda_2 \mathcal{L}_{\text{cond}}$ (50+ clinical constraints)
12	Merging	Weighted merge blocks with linear decay in overlaps: [B·N <sub>b</sub> , C, 32, 32, 24] $\rightarrow$ [B, C, D, H, W]
13	Update	AdamW ( $\eta_0 = 5 \times 10^{-4}$ , cosine decay to $10^{-6}$ )
14	Stop	Terminate if validation dose compliance plateaus for 20 epochs

---